

# First detection of methyl formate in the hot molecular core IRAS 18566+0408

Arijit Manna<sup>1</sup> • Sabyasachi Pal<sup>1</sup>

**Abstract** The studies of the complex molecular emission lines in the millimeter and submillimeter wavelengths towards the hot molecular cores reveal valuable details about the chemical complexity in the interstellar medium (ISM). We presented the first detection of the rotational emission lines of the complex organic molecule methyl formate ( $\text{CH}_3\text{OCHO}$ ) towards the hot molecular core region IRAS 18566+0408 using the high-resolution Atacama Large Millimeter/Submillimeter Array (ALMA) band 3 observation. The estimated column density of  $\text{CH}_3\text{OCHO}$  using the rotational diagram analysis was  $(4.1 \pm 0.1) \times 10^{15} \text{ cm}^{-2}$  with a rotational temperature of  $102.8 \pm 1.2 \text{ K}$ . The estimated fractional abundance of  $\text{CH}_3\text{OCHO}$  relative to hydrogen ( $\text{H}_2$ ) towards the IRAS 18566+0408 was  $3.90 \times 10^{-9}$ . We noted that the estimated fractional abundance of  $\text{CH}_3\text{OCHO}$  is fairly consistent with the simulation value predicted by the three-phase warm-up model from Garrod (2013). We also discussed the possible formation mechanism of  $\text{CH}_3\text{OCHO}$  towards the IRAS 18566+0408.

**Keywords** ISM: individual objects (IRAS 18566+0408) – ISM: abundances – ISM: kinematics and dynamics – stars: formation – astrochemistry

## 1 Introduction

The study of the hot molecular cores (HMCs), specially in the initial evolution phases, is difficult due to large distances ( $\geq 1 \text{ kpc}$ ), complex cluster environments, and short evolution timescales ( $\leq 10^4 \text{ years}$ ) (Silva et al. 2017). The HMCs are one of the early stages of star-formation, and

they play an important role in the ISM's chemical complexity (Shimonishi et al. 2021). The HMCs are mainly characterised by their small source size ( $\leq 0.1 \text{ pc}$ ), high temperature ( $\geq 100 \text{ K}$ ), and high gas density ( $n_{\text{H}_2} \geq 10^6 \text{ cm}^{-3}$ ) (van Dishoeck & Blake 1998). The HMC regions contain high-velocity  $\text{H}_2\text{O}$  masers that are located near Ultra-Compact (UC) H II regions (Mehring et al. 2004). The HMCs are the most chemically rich phase in the ISM and they are characterised by the presence of complex organic molecules like methyl cyanide ( $\text{CH}_3\text{CN}$ ), methyl isocyanate ( $\text{CH}_3\text{NCO}$ ), methyl formate ( $\text{CH}_3\text{OCHO}$ ), methanethiol ( $\text{CH}_3\text{SH}$ ), dimethyl ether ( $\text{CH}_3\text{OCH}_3$ ), methanol ( $\text{CH}_3\text{OH}$ ), ethyl cyanide ( $\text{C}_2\text{H}_5\text{CN}$ ), vinyl cyanide ( $\text{C}_2\text{H}_3\text{CN}$ ), methylamine ( $\text{CH}_3\text{NH}_2$ ), methylene imine ( $\text{CH}_2\text{NH}$ ), aminoacetonitrile ( $\text{NH}_2\text{CH}_2\text{CN}$ ), and cyanamide ( $\text{NH}_2\text{CN}$ ) etc (Silva et al. 2017; Beuther et al. 2002; Shimonishi et al. 2021; Hofner et al. 2017; Gorai et al. 2021; Ohishi et al. 2019; Manna & Pal 2022a,b). The phase of HMCs is thought to last about  $\sim 10^5 \text{ years}$  to  $\sim 10^6 \text{ years}$  (van Dishoeck & Blake 1998; Garrod & Herbst 2006).

The HMC candidate IRAS 18566+0408 (alternatively, G37.55+0.20) was located at a distance of 6.7 kpc (Sridharan et al. 2002). The far-infrared luminosity of IRAS 18566+0408 was  $\sim 8 \times 10^4 L_{\odot}$ , which originated from a single compact ( $\geq 5''$ ) dust continuum source (Silva et al. 2017). The single compact dust continuum emission towards IRAS 18566+0408 indicated the presence of an O8 ZAMS high-mass star (Zhang et al. 2007; Sridharan et al. 2002; Silva et al. 2017). Earlier, Carral et al. (1999) and Araya et al. (2005) detected the first weak radio continuum emission from IRAS 18566+0408 at wavelengths of 2 cm and 3.6 cm with a very low flux density  $\sim 0.7 \text{ mJy}$ , which indicated that this source is in the initial stage of the development of the UC H II region. Recently, Hofner et al. (2017) detected the radio continuum emission from IRAS 18566+0408, which was resolved into 1.3 cm and 6 cm wavelengths, and they claimed that the radio continuum emission is consistent with an ionised jet. The HMC object IRAS 18566+0408 was clas-

Arijit Manna

Sabyasachi Pal

<sup>1</sup>Midnapore City College, Kuturia, Bhadutala, Paschim Medinipur, West Bengal, 721129, India  
email: arijitmanna@mconline.org.in

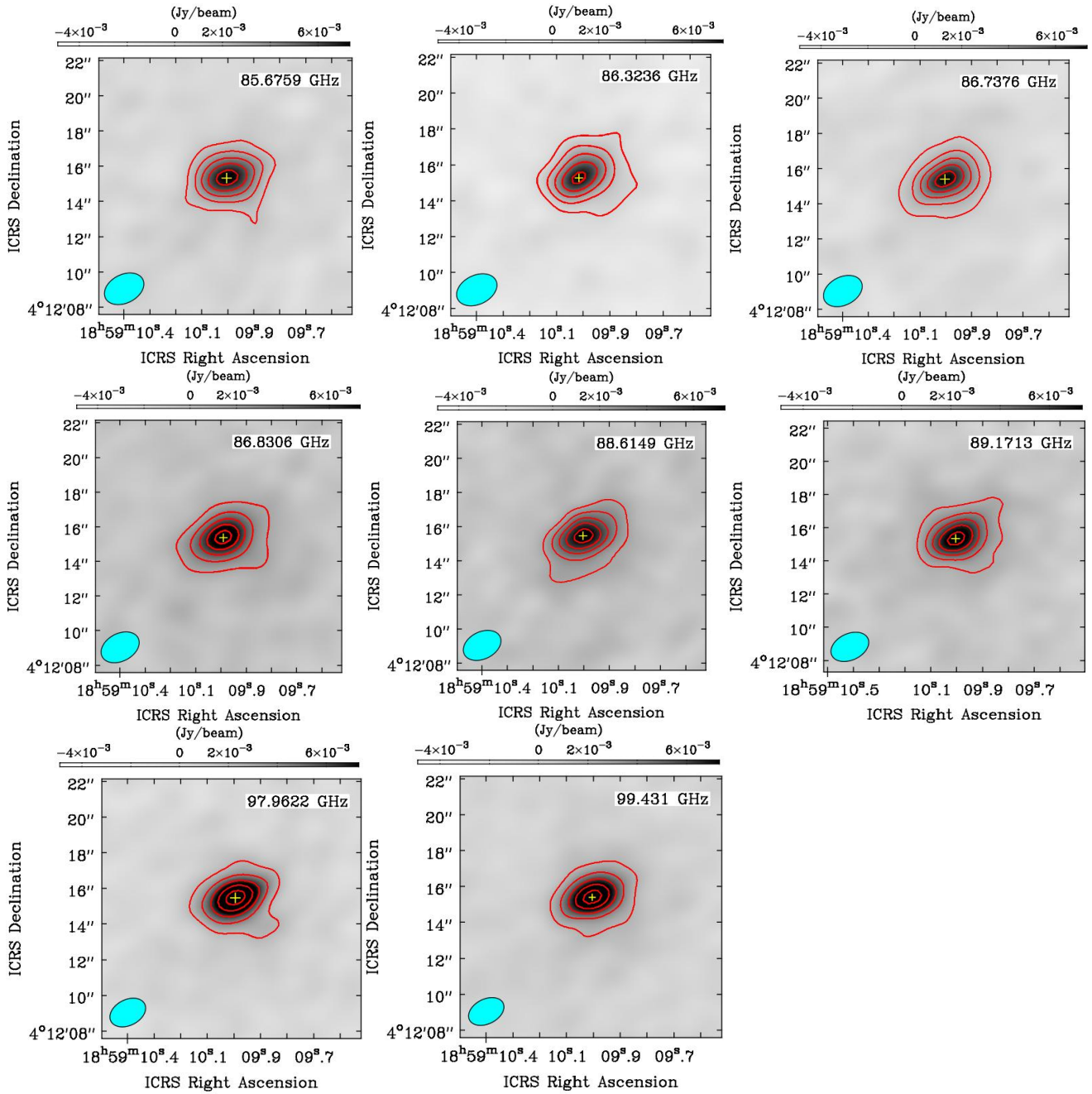


**Fig. 1** Continuum images of IRAS 18566+0408 obtained with ALMA at frequency (i) 85.6759 GHz ( $\sigma = 34.91 \mu\text{Jy beam}^{-1}$ ), (ii) 86.3236 GHz ( $\sigma = 43.31 \mu\text{Jy beam}^{-1}$ ), (iii) 86.7376 GHz ( $\sigma = 40.20 \mu\text{Jy beam}^{-1}$ ), (iv) 86.8305 GHz ( $\sigma = 40.75 \mu\text{Jy beam}^{-1}$ ), (v) 88.6148 GHz ( $\sigma = 31.93 \mu\text{Jy beam}^{-1}$ ), (vi) 89.1716 GHz ( $\sigma = 47.30 \mu\text{Jy beam}^{-1}$ ), (vii) 97.9621 GHz ( $\sigma = 45.39 \mu\text{Jy beam}^{-1}$ ), and (viii) 99.4310 GHz ( $\sigma = 28.99 \mu\text{Jy beam}^{-1}$ ). The contour levels started at  $3\sigma$ , where  $\sigma$  is the RMS of each continuum image, and the contour levels increased by a factor of  $\sqrt{2}$ . The cyan circles indicate the synthesised beam of the continuum images. The corresponding synthesised beam size of all continuum images was presented in Table. 1. The yellow cross-hair in the centre of each continuum map indicates the peak continuum position.

sified as a massive disk candidate (Zhang 2005). The emission lines of maser methanol ( $\text{CH}_3\text{OH}$ ) and water ( $\text{H}_2\text{O}$ ) at frequencies of 6.7 GHz and 22 GHz were strongly evident towards IRAS 18566+0408 (Beuther et al. 2002). The emission lines of maser formaldehyde ( $\text{H}_2\text{CO}$ ) at wavelength 6 cm were found from the IRAS 158566+0408 (Araya et al. 2005). The emission lines of ammonia ( $\text{NH}_3$ ) with transitions  $J = 1, 1$  and  $J = 2, 2$  were detected by the single-dish radio telescopes towards IRAS 18566+0408 (Miralles et al. 1994; Molinari et al. 1996; Sridharan et al. 2002) and later Zhang et al. (2007) studied details of the emitting region of  $\text{NH}_3$  towards IRAS 18566+0408 using the VLA.

In the ISM, the complex organic molecule methyl formate ( $\text{CH}_3\text{OCHO}$ ) was one of the most abundant organic molecular species, which was specially found in both high-mass and low-mass star formation regions (Brown et al. 1975; Cazaux et al. 2003). The emission lines of  $\text{CH}_3\text{OCHO}$  were first detected towards the Sgr B2(N) (Brown et al. 1975). Earlier, many chemical models indicated that the  $\text{CH}_3\text{OCHO}$  molecule was formed after the evaporation of the methanol ( $\text{CH}_3\text{OH}$ ) from the grain mantle towards HMCs (Millar et al. 1991). Garrod et al. (2008) presented the formation mechanism of  $\text{CH}_3\text{OCHO}$  in gas-grain interaction, but how to produce  $\text{CH}_3\text{OCHO}$  in the ISM using gas-phase reactions is not well understood. The emission lines of  $\text{CH}_3\text{OCHO}$  also detected towards another HMC candidate G31.41+0.31 with an estimated column density  $3.4 \times 10^{18} \text{ cm}^{-2}$  (Isokoski et al. 2013). The emission lines of  $\text{CH}_3\text{OCHO}$  were also seen in the low-mass protostar IRAS 16293–2422 (Cazaux et al. 2003). Earlier, Sakai et al. (2006) detected the emission lines of  $\text{CH}_3\text{OCHO}$  from NGC 1333 IRAS 4B, and the author claimed these molecules can be used as a tracer of complex biomolecules in the HMC regions. Therefore,  $\text{CH}_3\text{OCHO}$  was an important molecule on the grain surfaces of hot corinos and HMCs.

In this article, we presented the first detection of the rotational emission lines of  $\text{CH}_3\text{OCHO}$  towards IRAS 18566+0408 using ALMA band 3. This paper is organised as follows. In Section 2, we discussed the observations and data reductions. The result of the detection of  $\text{CH}_3\text{OCHO}$  was shown in Section 3. The discussion and summary were presented in Section 4 and 5.

## 2 Observations and data reduction

The millimeter-wavelength observation of HMC candidate IRAS 18566+0408 was performed with the Atacama Large Millimeter/Submillimeter Array (ALMA) using the band 3 (frequency range 85.64–100.42 GHz) receiver (Project code: 2015.1.00369.S., PI: Rosero, Viviana). The observed phase centre of IRAS 18566+0408 was  $\alpha_{J2000}$ : 18:59:10.000 and  $\delta_{J2000}$ : +04:12:16.000. During the observation, XX, YY, and XY-type signal correlators were

used via the integration times of 1360.800 Sec. The observations were made on March 24th, 2016 with a minimum baseline of 41 m and a maximum baseline of 216 m. During the observation, a total of thirty-six antennas were used to study the molecular lines from IRAS 18566+0408. The solar planet Neptune was taken as a flux calibrator, J1924–2914 was taken as a bandpass calibrator, and J1830+0619 was taken as a phase calibrator. The systematic velocity ( $V_{LSR}$ ) of IRAS 18566+0408 was  $\sim 84.5 \text{ km s}^{-1}$  (Silva et al. 2017).

We used the Common Astronomy Software Application (CASA 5.4.1)<sup>1</sup> for initial data reduction and spectral imaging with the standard ALMA data reduction pipeline (McMullin et al. 2007). The continuum flux density of the flux calibrator Neptune for each baseline was scaled and matched with the Butler-JPL-Horizons 2012 flux calibrator model with 5% accuracy using the CASA task SETJY (Butler 2012). Initially, we calibrated the bandpass and flux by flagging the bad data using the CASA pipeline with task `hi_fa_flagdata` and `hi_fa_bandpassflag`. After the initial data reduction, we split the target data using the task `MSTRANSFORM` with rest frequency in each spectral window. We used the task `UVCONTSUB` for the continuum subtraction procedure from the UV plane. After the continuum subtraction, we made the spectral images of IRAS 18566+0408 using the task `TCLEAN` with the rest frequency of each spectral window. After the creation of the spectral data cubes, we used the task `IMPBCOR` for the correction of the primary beam pattern in the synthesised images.

## 3 Results

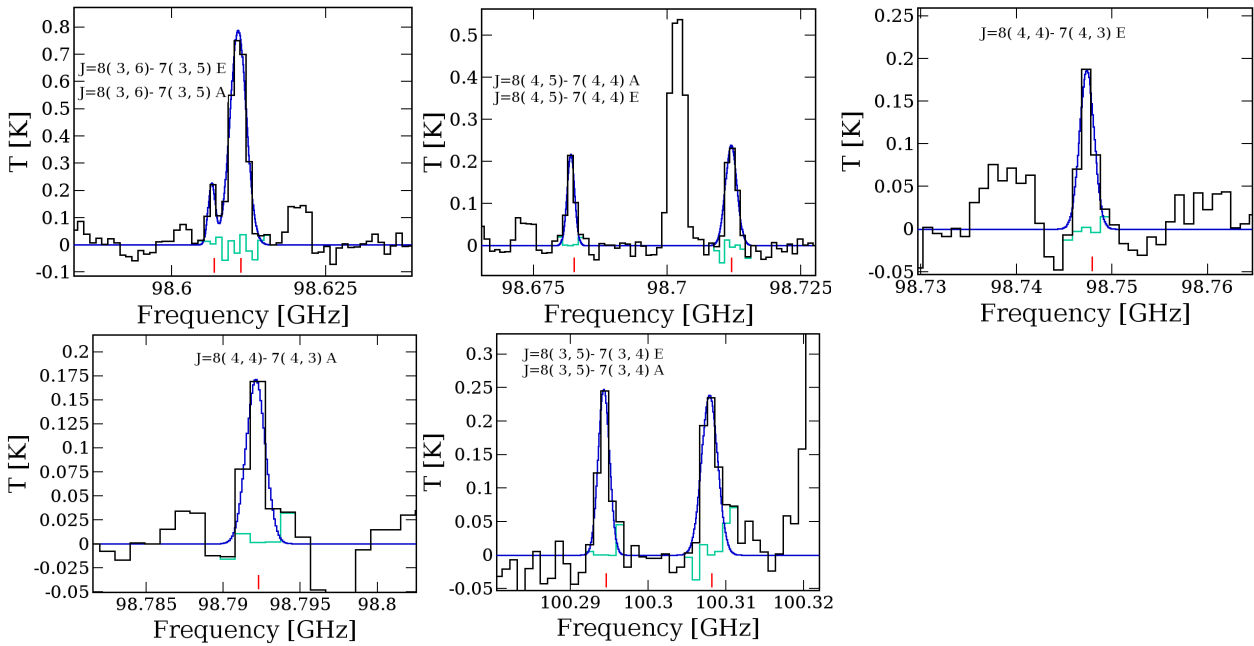
### 3.1 Continuum emission towards IRAS 18566+0408

We presented the millimeter wavelength continuum emission images towards IRAS 18566+0408 at frequencies of 85.6759 GHz (3.499 mm), 86.3236 GHz (3.472 mm), 86.7376 GHz (3.456 mm), 86.8305 GHz (3.452 mm), 88.6148 GHz (3.383 mm), 89.1716 GHz (3.361 mm), 97.9621 GHz (3.060 mm), and 99.4310 GHz (3.015 mm) in Figure 1, where the surface brightness colour scale has the unit of  $\text{Jy beam}^{-1}$ . After generating the continuum emission images, we used the CASA task `IMFIT` to fit the 2D Gaussian over the continuum images and obtained integrated flux density, peak flux density, synthesised beam size, position angle, and RMS, which are presented in Table 1. We observed that the continuum image of IRAS 18566+0408 was larger than the synthesised beam size for each image, which indicated that the millimeter wavelength continuum emission was resolved between the wavelength 3.015 mm–3.499 mm.

<sup>1</sup><https://casa.nrao.edu/>

**Table 1** Summary of the continuum images of IRAS 18566+0408.

Frequency (GHz)	Integrated flux (mJy)	Peak flux (mJy beam <sup>-1</sup> )	Beam size ("×")	Position angle (°)	RMS (μJy beam <sup>-1</sup> )
85.6759	13.53±0.66	7.16±0.24	2.399×1.622	-64.029	34.91
86.3236	11.49±0.94	6.58±0.36	2.382×1.618	-64.527	43.31
86.7376	10.47±0.53	6.40±0.22	2.377×1.603	-64.119	40.20
86.8305	13.01±0.89	7.74±0.35	2.386×1.601	-64.750	40.75
88.6148	12.19±0.94	6.81±0.35	2.336×1.588	-64.442	31.93
89.1716	10.68±0.52	7.19±0.23	2.323×1.578	-64.442	47.30
97.9621	17.02±1.10	10.14±0.45	2.131×1.442	-64.997	45.39
99.4310	16.81±0.99	9.43±0.38	2.099×1.377	-64.329	28.99

**Fig. 2** Rotational emission lines of CH<sub>3</sub>OCHO between the frequency range of 85.64–100.42 GHz with their different transitions towards IRAS 18566+0408. The continuum emission has been completely subtracted from the emission spectrum. The black line represented the observed emission spectra of CH<sub>3</sub>OCHO, while the blue line presented a Gaussian profile fitted to the observed spectra. The green line indicated the residual of the spectra.

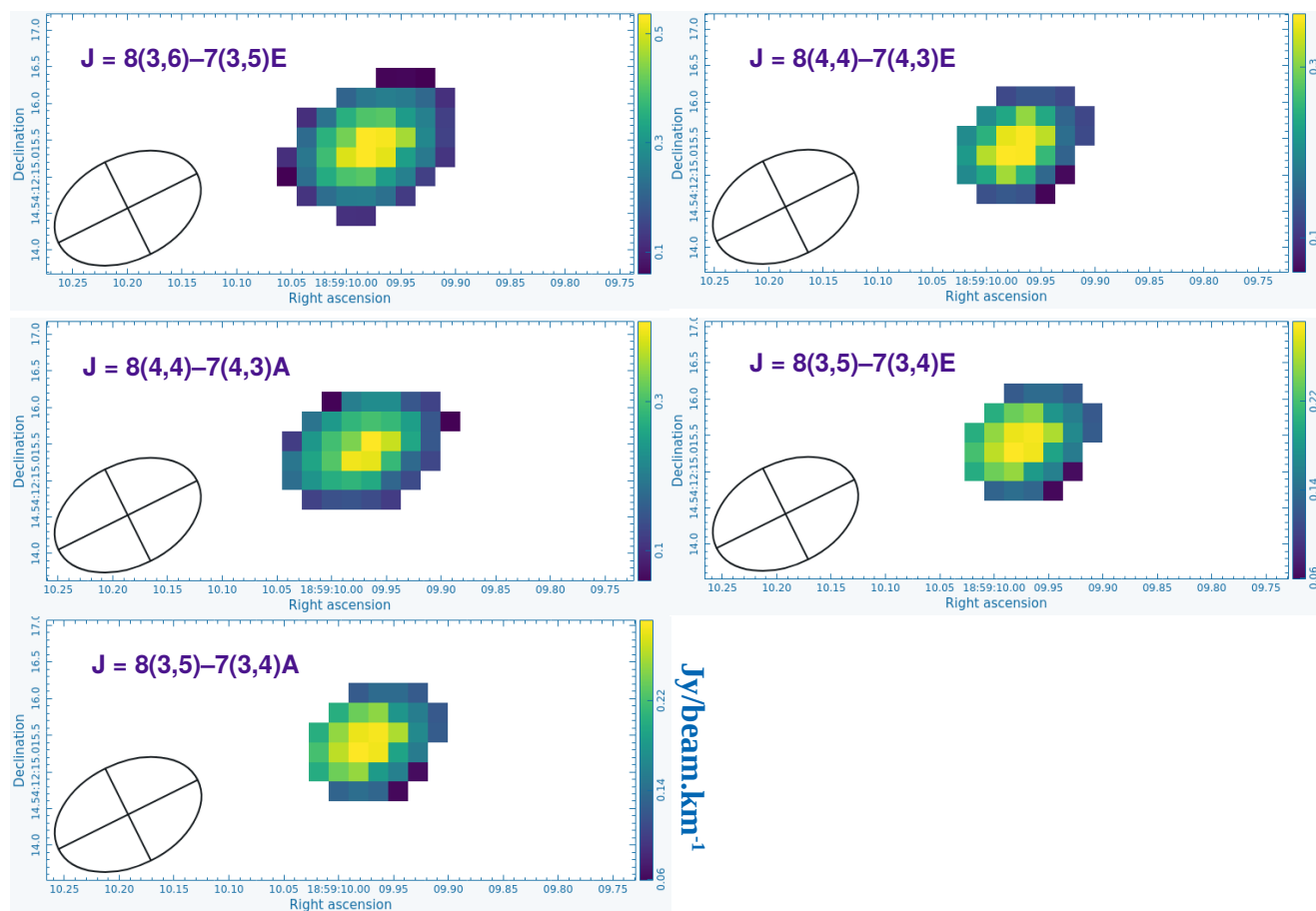


**Fig. 3** Integrated emission map of unblended transitions of  $\text{CH}_3\text{OCHO}$  towards IRAS 18566+0408. The black circles indicate the synthesised beam of the integrated emission map of  $\text{CH}_3\text{OCHO}$ . The black cross indicated the major and minor axis of the synthesised beam.

### 3.2 Estimation of hydrogen column density ( $N_{H_2}$ ) and optical depth ( $\tau_\nu$ ) towards IRAS 18566+0408

For optically thin dust continuum emission, the flux density ( $S_\nu$ ) can be expressed as,

$$S_\nu = \tau_\nu B_\nu(T_d) \Omega_{beam} \quad (1)$$

where,  $\tau_\nu$  indicated the optical depth,  $T_d$  is the dust temperature,  $B_\nu(T_d)$  presented the Planck function at dust temperature  $T_d$  (Whittet 1992), and  $\Omega_{beam} = (\pi/4 \ln 2) \times \theta_{major} \times \theta_{minor}$  was the solid angle of the synthesised beam. The equation of optical depth can be written as,

$$\tau_\nu = \rho_d \kappa_\nu L \quad (2)$$

where,  $\rho_d$  presented the mass density of dust,  $\kappa_\nu$  was the mass absorption coefficient, and  $L$  indicated the path length. The mass density of the dust can be expressed in terms of the dust-to-gas mass ratio ( $Z$ ),

$$\rho_d = Z \mu_H \rho_{H_2} = Z \mu_H N_{H_2} 2m_H / L \quad (3)$$

where,  $\mu_H$  indicated the mean atomic mass per hydrogen,  $\rho_{H_2}$  is the mass density of hydrogen,  $m_H$  is the mass of hydrogen, and  $N_{H_2}$  is the column density of hydrogen. We used dust temperature  $T_d = 170$  K (Hofner et al. 2017),  $\mu_H = 1.41$ , and  $Z = 0.01$  (Cox & Pilachowski 2000). The estimated peak flux density of the dust continuum of the IRAS 18566+0408 at different frequencies is presented in Table. 1. From equations 1, 2, and 3, the column density of molecular hydrogen can be expressed as,

$$N_{H_2} = \frac{S_\nu / \Omega}{2 \kappa_\nu B_\nu(T_d) Z \mu_H m_H} \quad (4)$$

During the estimation of the mass absorption coefficient ( $\kappa_\nu$ ), we adopted the formula  $\kappa_\nu = 0.90(\nu/230\text{GHz})^\beta \text{ cm}^2 \text{ g}^{-1}$  (Motogi et al. 2019), where  $k_{230} = 0.90 \text{ cm}^2 \text{ g}^{-1}$  indicated the emissivity of the dust grains at a gas density of  $10^6 \text{ cm}^{-3}$ , which covered by a thin ice mantle at 230 GHz. We used

**Table 2** Column density of hydrogen and optical depth.

Wavelength (mm)	Hydrogen column density ( $\text{cm}^{-2}$ )	Optical depth ( $\tau_\nu$ )
3.499	$1.18 \times 10^{24}$	0.00495
3.472	$1.05 \times 10^{24}$	0.00457
3.456	$1.01 \times 10^{24}$	0.00445
3.452	$1.21 \times 10^{24}$	0.00538
3.383	$9.64 \times 10^{23}$	0.00473
3.361	$1.01 \times 10^{24}$	0.00501
3.060	$1.06 \times 10^{24}$	0.00702
3.015	$9.42 \times 10^{23}$	0.00656
Average Value	$1.05 \times 10^{24}$	0.00533

the dust spectral index  $\beta \sim 1.3$  (Zhang et al. 2007; Silva et al. 2017). Using the adopted mass absorption coefficient formula, we obtained the value  $\kappa_\nu$  is 0.249, 0.251, 0.253, 0.254, 0.260, 0.262, 0.296, and 0.302 for the frequencies 85.6759 GHz, 86.3236 GHz, 86.7376 GHz, 86.8305 GHz, 88.6148 GHz, 89.1716 GHz, 97.9621 GHz, and 99.4310 GHz respectively. We estimated the column density of hydrogen for the eight frequency regions towards IRAS 18566+0408 which was presented in Table. 2. We take the average value to determine the resultant hydrogen column density towards IRAS 18566+0408. The obtained column density of hydrogen towards IRAS 18566+0408 was  $\sim 1.05 \times 10^{24} \text{ cm}^{-2}$ , which was estimated by taking the average of these eight continuum values. After the estimation of the hydrogen column density, we also estimated the value of optical depth ( $\tau_\nu$ ) using the following equation,

$$T_{mb} = T_d(1 - \exp(-\tau_\nu)) \quad (5)$$

where,  $T_{mb}$  indicated the brightness temperature and  $T_d$  is the dust temperature of IRAS 18566+0408. During the estimation of the brightness temperature, we used the Rayleigh-Jeans approximation,  $1 \text{ Jy beam}^{-1} \equiv 118 \text{ K}$ . The estimated dust optical depth of eight individual frequency regions was presented in Table. 2. The average dust optical depth is estimated to be 0.00533. The estimated dust optical depth indicated that the HMC candidate IRAS 18566+0408 is optically thin between the frequency range of 85.64–100.42 GHz.

### 3.3 Line emission towards IRAS 18566+0408

We extracted the millimeter wavelength spectra of IRAS 18566+0408 to create a  $2.5''$  diameter circular region centred at RA (J2000) = ( $18^h 59^m 09^s.92$ ), Dec (J2000) = ( $4^\circ 12' 15''.58$ ). After the extraction of the millimeter wavelength spectra, we used the CASSIS<sup>2</sup> (Vastel et al. 2015) for the identification of the molecular emission lines towards IRAS 18566+0408 using the Cologne Database for Molecular Spectroscopy (CDMS)<sup>3</sup> (Müller et al. 2005) or Jet Propulsion Laboratory (JPL)<sup>4</sup> (Pickett et al. 1998) spectroscopic molecular databases. After the spectral analysis using the Line Analysis module in CASSIS, we detected rotational emission lines of  $\text{CH}_3\text{OCHO}$  towards the IRAS 18566+0408 between the frequency ranges of 85.64–100.42 GHz with a spectral resolution of 1128.91 kHz. We identified a total of eight strong rotational transition lines of  $\text{CH}_3\text{OCHO}$  towards IRAS 18566+0408. There were no missing transition lines of  $\text{CH}_3\text{OCHO}$  within the observed frequency range.

<sup>2</sup><http://cassis.irap.omp.eu/?page=cassis>

<sup>3</sup><https://cdms.astro.uni-koeln.de/cgi-bin/cdmssearch>

<sup>4</sup><https://spec.jpl.nasa.gov/>

**Table 3** Summary of the line parameters of CH<sub>3</sub>OCHO towards IRAS 18566+0408.

Species	Frequency [GHz]	Transition [ $J'_{K'_a K'_c} - J''_{K''_a K''_c}$ ]	$E_u$ [K]	$A_{ij}$ [s <sup>-1</sup> ]	Peak intensity [K]	$S\mu^2$ [Debye <sup>2</sup> ]	FWHM [km s <sup>-1</sup> ]	$V_{LSR}$ [km s <sup>-1</sup> ]	$\int T_{mb} dV$ [K km s <sup>-1</sup> ]	Remark
CH <sub>3</sub> OCHO	98.6069	8(3,6)–7(3,5)E	27.26	$1.20 \times 10^{-5}$	0.211	18.246	5.230±0.31	84.50±0.25	1.287±0.32	Non blended
CH <sub>3</sub> OCHO	98.6112	8(3,6)–7(3,5)A	27.24	$1.20 \times 10^{-5}$	0.748	18.273	7.665±0.69	84.15±0.31	7.334±0.96	Blended with C <sub>2</sub> H <sub>5</sub> CN
CH <sub>3</sub> OCHO	98.6826	8(4,5)–7(4,4)A	31.89	$1.05 \times 10^{-5}$	0.212	15.966	7.658±1.23	84.21±0.55	1.358±0.29	Blended with NCCONH <sub>2</sub>
CH <sub>3</sub> OCHO	98.7120	8(4,5)–7(4,4)E	31.90	$1.02 \times 10^{-5}$	0.227	15.436	7.628±0.75	84.38±0.92	1.256±0.39	Blended with NCCONH <sub>2</sub>
CH <sub>3</sub> OCHO	98.7479	8(4,4)–7(4,3)E	31.91	$1.02 \times 10^{-5}$	0.187	15.440	6.682±0.98	84.18±0.86	1.287±0.21	Non blended
CH <sub>3</sub> OCHO	98.7923	8(4,4)–7(4,3)A	31.89	$1.05 \times 10^{-5}$	0.171	15.963	7.289±1.28	84.26±0.68	2.361±0.82	Non blended
CH <sub>3</sub> OCHO	100.2946	8(3,5)–7(3,4)E	27.41	$1.26 \times 10^{-5}$	0.245	18.259	6.289±0.98	84.30±0.86	8.172±1.83	Non blended
CH <sub>3</sub> OCHO	100.3082	8(3,5)–7(3,4)A	27.40	$1.26 \times 10^{-5}$	0.239	18.283	6.325±0.82	84.31±0.96	8.372±1.98	Non blended

After the identification of emission lines of CH<sub>3</sub>OCHO from the millimeter spectra of IRAS 18566+0408, we fitted the Gaussian model over the observed spectra of CH<sub>3</sub>OCHO using the line analysis module in CASSIS. We estimated the Full-Width Half Maximum (FWHM), quantum numbers ( $J'_{K'_a K'_c} - J''_{K''_a K''_c}$ ), upper state energy ( $E_u$ ), Einstein coefficients ( $A_{ij}$ ), peak intensity and integrated intensity ( $\int T_{mb} dV$ ) after fitting a Gaussian model over the observed spectra of CH<sub>3</sub>OCHO. The summary of the detected transitions of CH<sub>3</sub>OCHO and Gaussian fitting parameters of CH<sub>3</sub>OCHO was presented in Table 3 and the observed spectra of CH<sub>3</sub>OCHO with Gaussian fitting were shown in Figure 2. In the case of CH<sub>3</sub>OCHO, the torsional substates are noticed due to the internal rotation of the methyl group. So, we observed the A and E sub-states of CH<sub>3</sub>OCHO. We carefully checked for the possible line contamination in the spectral profiles of CH<sub>3</sub>OCHO with nearby molecular transitions during the spectral analysis using the line analysis module in CASSIS. We observed that  $J = 8(3,6) - 7(3,5)A$ ,  $J = 8(4,5) - 7(4,4)A$ , and  $J = 8(4,5) - 7(4,4)E$  transition lines of CH<sub>3</sub>OCHO blended with C<sub>2</sub>H<sub>5</sub>CN and NCCONH<sub>2</sub> respectively. The  $J = 8(4,4) - 7(4,3)A$  transition line of CH<sub>3</sub>OCHO does not have a proper Gaussian shape due to lower spectral resolution, but this transition is not blended with other nearby molecular transitions.

### 3.4 Spatial distribution of CH<sub>3</sub>OCHO towards IRAS 18566+0408

We created the integrated emission map of CH<sub>3</sub>OCHO using the task IMMOMENTS in CASA. The integrated emission maps were created by integrating the spectral data cubes in

**Table 4** Estimated emitting regions of CH<sub>3</sub>OCHO towards IRAS 18566+0408.

Molecule	Transition [ $J'_{K'_a K'_c} - J''_{K''_a K''_c}$ ]	Emitting region ["]
CH <sub>3</sub> OCHO	8(3,6)–7(3,5)E	1.129
	8(4,4)–7(4,3)E	1.120
	8(4,4)–7(4,3)A	1.213
	8(3,5)–7(3,4)E	1.135
	8(3,5)–7(3,4)A	1.133

the velocity range where the emission lines of CH<sub>3</sub>OCHO were detected. We created the emission map only for the unblended transition lines of CH<sub>3</sub>OCHO. The integrated emission map was shown in Figure 3, which was created using the Cube Analysis and Rendering Tool for Astronomy (CARTA)<sup>5</sup> software package (Comrie et al. 2021). The resultant emission map indicated that the emission lines of CH<sub>3</sub>OCHO arise from the warm inner region of IRAS 18566+0408. After the generation of the emission map, we fitted a 2D Gaussian over the integrated map using CASA task IMFIT. The deconvolved beam size of the emitting region was calculated from the following equation

$$\theta_s = \sqrt{\theta_{50}^2 - \theta_{beam}^2} \quad (6)$$

where  $\theta_{50} = 2\sqrt{A/\pi}$  indicated the diameter of the circle whose area was enclosing 50% line peak and  $\theta_{beam}$  indicated the half-power width of the synthesised beam (Manna & Pal 2022a,b). The estimated emitting region of unblended transitions of CH<sub>3</sub>OCHO is presented in Table 4. The emitting region of CH<sub>3</sub>OCHO varies between 1.120''–1.213''. We noticed that the emitting region of CH<sub>3</sub>OCHO is smaller than the synthesised beam size, which indicates all transitions of CH<sub>3</sub>OCHO were not spatially resolved.

### 3.5 Rotational diagram analysis

We have detected the multiple hyperfine transitions of CH<sub>3</sub>OCHO with different upper-state energies ( $E_u$ ). So, we used the rotational diagram method to obtain the column density ( $N$ ) in cm<sup>-2</sup> and rotational temperature ( $T_{rot}$ ) in K of detected emission lines of CH<sub>3</sub>OCHO towards IRAS 18566+0408. We used the rotational diagram method because we assumed that the observed molecular emission lines were optically thin and that they were populated in Local Thermodynamic Equilibrium (LTE) conditions. The assumption of LTE condition was reasonable towards the IRAS 18566+0408 due to very high gas density ( $2.6 \times 10^7$  cm<sup>-3</sup> in the inner regions of hot core (Silva et al. 2017)). We

<sup>5</sup><https://carta.readthedocs.io/en/latest/introduction.html>

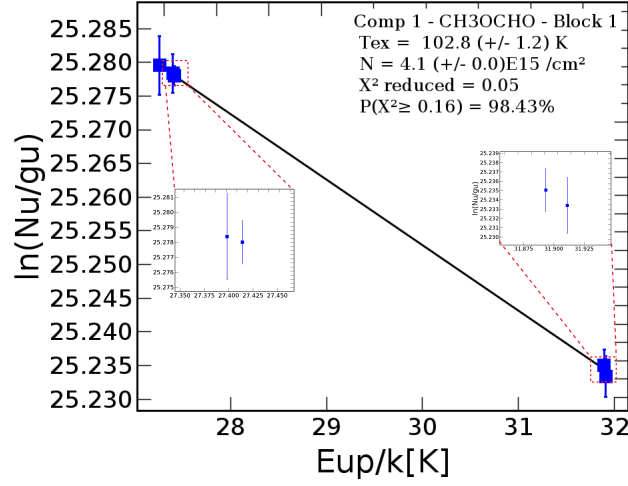


**Fig. 4** Rotational diagram of CH<sub>3</sub>OCHO towards IRAS 18566+0408. The blue blocks indicated the statistical data points, and the solid black lines presented the fitted straight lines which estimated the column density and rotational temperature. The vertical blue error bars were the absolute uncertainty of  $\ln(N_u/g_u)$ .

observed the last four unblended transitions of CH<sub>3</sub>OCHO, i.e.,  $J = 8(4,4)-7(4,3)E$  ( $E_u = 31.91$  K),  $J = 8(4,4)-7(4,3)A$  ( $E_u = 31.89$  K),  $J = 8(3,5)-7(3,4)E$  ( $E_u = 27.41$  K), and  $J = 8(3,5)-7(3,4)A$  ( $E_u = 27.40$  K) consist of two close pairs in the upper state energy ( $E_u$ ) levels. These four transitions exist in the same  $J$  group but they are separated by two rotational sub-states, A and E, which occur due to internal molecular rotation of the methyl (CH<sub>3</sub>) group (Sakai et al. 2015). The line intensities of the A and E sublevels of CH<sub>3</sub>OCHO are nearly similar (Sakai et al. 2015). The rotational diagram and LTE modelling do not affect the types of CH<sub>3</sub>OCHO transitions. The column density of optically thin molecular emission lines can be expressed as (Goldsmith & Langer 1999),

$$N_u^{thin} = \frac{3g_u k_B \int T_{mb} dV}{8\pi^3 \nu S \mu^2} \quad (7)$$

where,  $g_u$  presented the degeneracy of the upper state energy ( $E_u$ ),  $k_B$  is the Boltzmann constant,  $\int T_{mb} dV$  indicated the integrated intensity of the detected emission lines,  $\mu$  is the electric dipole moment,  $S$  is the strength of the transition lines, and  $\nu$  is the rest frequency of observed molecules. Under the LTE conditions, the column density of the detected molecules can be expressed as,

$$\frac{N_u^{thin}}{g_u} = \frac{N_{total}}{Z(T_{rot})} \exp(-E_u/k_B T_{rot}) \quad (8)$$

where,  $T_{rot}$  is the rotational temperature,  $Z(T_{rot})$  is the partition function at extracted rotational temperature, and  $E_u$  is the upper state energy of the observed molecules. Equation

8 can be rearranged as,

$$\ln\left(\frac{N_u^{thin}}{g_u}\right) = \ln(N) - \ln(Z) - \left(\frac{E_u}{k_B T_{rot}}\right) \quad (9)$$

Equation 9 demonstrated the linear relationship between the  $E_u$  and  $\ln(N_u/g_u)$ . The column density and rotational temperature can be estimated by fitting a straight line to the values of  $\ln(N_u/g_u)$  which is plotted as a function of  $E_u$ . The value of  $N_u/g_u$  is estimated from equation 7. For the rotational diagram analysis, we extracted the line parameters like FWHM, upper state energy ( $E_u$ ), line intensity, and integrated intensity ( $\int T_{mb} dV$ ) using a Gaussian fitting over the observed spectra of CH<sub>3</sub>OCHO which was presented in Table 3. During the rotational diagram analysis, we used only unblended transitions of the detected species. The computed rotational diagram of CH<sub>3</sub>OCHO was shown in Figure 4. In the rotational diagram, the vertical blue error bars were the absolute uncertainty of  $\ln(N_u/g_u)$ , and it was generated from the error of the observed  $\int T_{mb} dV$ , which was measured using the fitting of Gaussian model over observed transitions of CH<sub>3</sub>OCHO. Using the rotational diagram analysis, we found the column density of CH<sub>3</sub>OCHO was  $(4.1 \pm 0.1) \times 10^{15} \text{ cm}^{-2}$  with rotational temperature  $102.8 \pm 1.2$  K. The estimated rotational temperatures of CH<sub>3</sub>OCHO are similar to the typical hot core temperature since the temperature of the hot core is above 100 K (van Dishoeck & Blake 1998). After the estimation of the column density, we estimated the fractional abundance of CH<sub>3</sub>OCHO which was  $3.90 \times 10^{-9}$ . The fractional abundance of CH<sub>3</sub>OCHO was estimated with respect to H<sub>2</sub>, where the column density of H<sub>2</sub> towards IRAS 18566+0408 was  $1.05 \times 10^{24} \text{ cm}^{-2}$  (see Section. 3.2).



**Table 5** Comparison between the simulated and observed fractional abundance of CH<sub>3</sub>OCHO.

Species	Simulated Values <sup>a</sup>						Observed Values <sup>b</sup>	
	Fast		Medium		Slow		IRAS 18566+0408	
	Abundance	T (K)	Abundance	T (K)	Abundance	T (K)	Abundance	T (K)
CH <sub>3</sub> OCHO	$9.2 \times 10^{-8}$	120	$3.7 \times 10^{-8}$	111	$3.1 \times 10^{-9}$	103	$3.90 \times 10^{-9}$	102.8

Notes: a – Values taken from Table 8 of Garrod (2013);

b – this work.

#### 4 Discussion

Here, we presented a comparison between observational results and existing astrochemical simulations of CH<sub>3</sub>OCHO. We followed the three-phase warm-up model of Garrod (2013) to compare the observational and simulation results. Garrod (2013) considered an isothermal collapse phase, which was followed by a static warm-up phase. In the first phase, the number density increased from  $n_H = 3 \times 10^3$  to  $10^7$  cm<sup>-3</sup> under the free-fall collapse, and the dust temperature was reduced to 8 K from 16 K. In the second phase, the density remained fixed at  $\sim 10^7$  cm<sup>-3</sup> where the dust temperature fluctuated from 8 K to 400 K. The temperature of IRAS 18566+0408 was  $\sim 170$  K, which is a typical hot core temperature, and the number density ( $n_H$ ) of this source is  $2.6 \times 10^7$  cm<sup>-3</sup> (Hofner et al. 2017; Silva et al. 2017). Thus, the hot core model of Garrod (2013) is suitable for understanding the chemical evolution towards the IRAS 18566+0408. Garrod (2013) used the fast, medium, and slow warm-up models based on different time scales. The time scale of the fast warm-up model is more suitable for studying the chemical evolution of HMC regions (Gorai et al. 2021). In Table 5, we compare the observed fractional abundance of CH<sub>3</sub>OCHO with the simulated abundance results of Garrod (2013) and we noticed that the slow warm-up model of Garrod (2013) satisfied our estimated abundance of CH<sub>3</sub>OCHO towards IRAS 18566+0408. Garrod (2013) estimated that the abundance of CH<sub>3</sub>OCHO towards the HMCs environment is  $3.1 \times 10^{-9}$  with temperature 103 K under the slow warm-up conditions and we estimated the abundance of CH<sub>3</sub>OCHO towards HMC object IRAS 18566+0408 was  $3.90 \times 10^{-9}$  with temperature 102.8 K, which indicated a good agreement between the simulation and observational results.

In the ISM, the CH<sub>3</sub>OCHO molecule can be efficiently created on the surface of dust grains via the reaction between methoxy radical (CH<sub>3</sub>O) and formyl radical (HCO) (HCO+CH<sub>3</sub>O→CH<sub>3</sub>OCHO). This reaction is the main formation route in the three-phase warm-up chemical model by Garrod (2013). The chemical simulation between CH<sub>3</sub>O and HCO shows that these radicals are mobile around 30–40 K and the reaction is efficient for the formation of CH<sub>3</sub>OCHO in the HMCs (Garrod 2013). According to the simulation of Figure 1 in Garrod (2013), it is clear that the gas phase

CH<sub>3</sub>OCHO in the HMC region mainly comes from the ice phase. Our estimated abundance of CH<sub>3</sub>OCHO ( $3.90 \times 10^{-9}$ ) towards IRAS 18566+0408 is similar to the simulated abundance of CH<sub>3</sub>OCHO ( $3.91 \times 10^{-9}$ ) under the slow warm-up model of Garrod (2013), which indicated that CH<sub>3</sub>O and HCO are responsible for the production of CH<sub>3</sub>OCHO on the surface of dust grains in IRAS 18566+0408. The slow-warm phase of CH<sub>3</sub>OCHO indicated that a significant amount of CH<sub>3</sub>OCHO is destroyed due to the evaporation of the methanol (CH<sub>3</sub>OH) in the hot core region of IRAS 18566+0408.

#### 5 Summary

In this article, we presented the detection of complex biomolecule CH<sub>3</sub>OCHO at millimeter wavelengths towards the HMC candidate IRAS 18566+0408 using the ALMA. The main results are as follows.

- We reported the first detection of the rotational emission lines of CH<sub>3</sub>OCHO towards the HMC region IRAS 18566+0408 using ALMA band 3 between the frequency range of 85.64–100.42 GHz.
- From the dust continuum emission, the estimated column density of hydrogen ( $N_{H_2}$ ) was  $1.05 \times 10^{24}$  cm<sup>-2</sup>. We also estimated that the dust optical depth was 0.00533, which indicated IRAS 18566+0408 is optically thin between the frequency range of 85.64–100.42 GHz.
- The estimated column density of CH<sub>3</sub>OCHO towards IRAS 18566+0408 was  $(4.1 \pm 0.1) \times 10^{15}$  cm<sup>-2</sup> with rotational temperature  $102.8 \pm 1.2$  K. The estimated fractional abundance of CH<sub>3</sub>OCHO towards IRAS 18566+0408 with respect to H<sub>2</sub> is  $3.90 \times 10^{-9}$ . Our estimated rotational temperature indicated that the emission lines of CH<sub>3</sub>OCHO arise from the warm inner region of IRAS 18566+0408 because the temperature of the hot core, in general, is above 100 K.
- We compared our estimated abundance of CH<sub>3</sub>OCHO with the three-phase warm-up model of Garrod (2013). After the comparison, we noticed that the slow warm-up model of Garrod (2013) satisfied the abundance of CH<sub>3</sub>OCHO towards IRAS 18566+0408.
- After the successful detection of CH<sub>3</sub>OCHO towards IRAS 18566+0408, a broader study was needed to search for other molecular lines in the other frequency bands of ALMA to understand the chemical complexity in this HMC.

## Acknowledgments

We thank the anonymous referee for the helpful comments that improved the manuscript. This paper makes use of the following ALMA data: ADS/JAO.ALMA#2015.1.00369.S (PI: Rosero, Viviana). ALMA is a partnership of ESO (representing its member states), NSF (USA), and NINS (Japan), together with NRC (Canada), MOST and ASIAA (Taiwan), and KASI (Republic of Korea), in co-operation with the Republic of Chile. The Joint ALMA Observatory is operated by ESO, AUI/NRAO, and NAOJ.

## Data availability

The data that support the plots within this paper and other findings of this study are available from the corresponding author upon reasonable request. The raw ALMA data are publicly available at <https://almascience.nao.ac.jp/asax/> (project id: 2015.1.00369.S).

## Funding

No funds or grants were received during the preparation of this manuscript.

## Conflicts of interest

The authors declare no conflict of interest.

## Author Contributions

S.P. conceptualize the project. A.M. analysed the ALMA data and identify the emission lines of methyl formate (CH<sub>3</sub>OCHO) from HMC candidate IRAS 18566+0408. A.M. analyses the rotational diagram to derive the column density and rotational temperature of CH<sub>3</sub>OCHO. A.M. and S.P. wrote the main manuscript text. All authors reviewed the manuscript.

## References

Araya, E., Hofner, P., Kurtz, S., et al. 2005, *ApJ*, 618, 339  
 Balucani N., Ceccarelli C., Taquet V. 2015, *MNRAS*, 449, L16  
 Butler B. 2012, ALMA Memo Series, NRAO  
 Bonfand, M., Belloche, A., Garrod, R.T., et al. 2019, *A&A*, 628, A27  
 Brown, R.D., Crofts, J.G., Godfrey, P. D., et al. 1975, *ApJ*, 197, L29

Beuther H., Schilke P., Sridharan T. K., et al. 2002, *A&A*, 383, 892  
 Comrie, A., Wang, K.-S., Ford, P., et al. 2021, CARTA: The Cube Analysis and Rendering Tool for Astronomy, 1.3.0, Zenodo  
 Cazaux, S., Tielens, A. G. G. M., Ceccarelli, C., et al. 2003, *A&A*, 593, L51  
 Carral, P., Kurtz, S., Rodriguez, L. F., et al. 1999, *RMxAA*, 35, 97  
 Cox, A. N., & Pilachowski, C. A. 2000, *Physics Today*, 53, 77  
 Garrod, R. T., & Herbst, E. 2006, *A&A*, 457, 927  
 Garrod, R. T., Weaver, S. L. W., & Herbst, E. 2008, *ApJ*, 682, 283  
 Garrod R. T. 2013, *ApJS*, 765, 60  
 Goldsmith, P. F., & Langer, W. D. 1999, *ApJ*, 517, 209  
 Gorai, P., Das, A., Shimonishi, T., et al. 2021, *ApJ*, 907, 108.  
 Hofner P., Cesaroni R., Kurtz S., et al. 2017, *ApJ* 843 99  
 Isokoski K., Bottinelli S., & van Dishoeck E. F. 2013, *A&A*, 554, A100  
 Manna, A. & Pal, S., 2022, *Life Sciences in Space Research*, 34, 9  
 Manna, A. & Pal, S., 2022, *Journal of Astrophysics and Astronomy*, 43, 83  
 Mehringer, D. M., Pearson, J. C., Keene, J., & Phillips, T. G. 2004, *ApJ*, 608,306-313  
 Motogi, K., Hirota, T., Machida, M. N., et al. 2019, *ApJL*, 877, L25  
 Molinari S., Brand J., Cesaroni R., & Palla, F., 1996, *A&A*, 308, 573  
 Miralles M. P., Rodriguez L. F., & Scalise, E. 1994, *ApJS*, 92, 173  
 McMullin, J. P., Waters, B., Schiebel, D., et al. 2007, San Francisco, CA: ASP, 127  
 Millar, T. J., Herbst, E., & Charnley, S. B. 1991, *ApJ*, 369, 147  
 Müller, H. S. P., Schlmöder, F., Stutzki, J. & Winnewisser, G. 2005, *Journal of Molecular Structure*, 742, 215–227  
 Ohishi, M., Suzuki, T., Hirota, T., Saito, M. & Kaifu, N. 2019, *PASJ*, 71  
 Pickett, H. M., Poynter, R. L., Cohen, E. A., et al. 1998, *Journal of Quantitative Spectroscopy and Radiative Transfer*, 60, 883  
 Silva A., Zhang Q., Sanhueza P., et al. 2017, *ApJ*, 847, 1538  
 Sridharan T. K., Beuther H., Schilke P., et al. 2002, *ApJ*, 566, 931  
 Shimonishi, T., Izumi, N., Furuya, K., & Yasui, C., 2021, *ApJ*, 2, 206  
 Sakai, Y., Kobayashi, K., & Hirota, T. 2015, *ApJ*, 803, 97  
 Sakai, N., Sakai, T., Yamamoto, S. 2006, *PASJ*, 58, L15  
 van Dishoeck E. F., & Blake G. A. 1998, *Annu Rev Astron Astrophys*, 36, 317  
 Vastel, C., Bottinelli, S., Caux, E., et al. 2015, *Proceedings of the Annual meeting of the French Society of Astronomy and Astrophysics*, 313-316  
 Whittet, D. C. B. 1992, *Journal of the British Astronomical Association*, 102, 230  
 Zhang Q., 2005, in *Massive Star Birth: A Crossroads of Astrophysics*, ed. R. Cesaroni et al. (Cambridge: Cambridge Univ. Press), 135  
 Zhang Q., Sridharan T. K., Hunter T. R., et al., 2007, *A&A*, 470, 269